



GEOSCIENCES

Concentration and thickness of sea ice in the Weddell Sea from SSM/I passive microwave radiometer data

FERNANDO LUIS HILLEBRAND, MARCOS W.D. DE FREITAS, ULISSES F. BREMER, TALES C. ABRANTES, JEFFERSON C. SIMÕES, CLÁUDIO W. MENDES JÚNIOR, FREDERICO SCHARDONG & JORGE ARIGONY-NETO

Abstract: This study evaluated feasibility statistically and analyzed, during the freezing period, the relationship between brightness temperature (T_b) data of the 37V polarisation and the GR3719 (Gradient Ratio 37V and 19V) obtained by Special Sensor Microwave/Imager from F11 and F13 satellites with sea ice thickness (SIT) data obtained in the Weddell Sea through Antarctic Sea Ice Processes and Climate program. The multiple linear regression (MLR) was applied at 1,520 points, with 70% of these points being randomly separated to generate the MLR and 30% to carry out the validation. To perform the temporal mapping, the MLR was applied only to pixels with sea ice concentration (SIC) $\geq 90\%$, obtained through the fraction image calculated from the spectral linear mixing model (SLMM) using the T_b in the channels and polarizations 19H, 19V and 37V. The results of the SLMM validation process for estimating the SIC were $\sigma = 10.5\%$, $RMSE = 11.0\%$, and bias = -2.8% , and the SIT based on the MLR, the results were $R^2 = 0.57$, $RMSE = 0.268$ m, and bias = 0.103 m. In the SIT mapping, we highlight the trend of thickness reduction on the east coast of the Antarctic Peninsula during the period 1992–2009.

Key words: Spectral linear mixing model, multiple linear regression, sea ice concentration, brightness temperature.

INTRODUCTION

The distribution of sea ice thickness (SIT) is a fundamental parameter in the Earth's climate system and an essential component in ocean-atmosphere interactions controlling the energy and salinity balances in the polar regions (Ozsoy-Cicek et al. 2013, Renner & Lytle 2007). By using the SIT combined with the sea ice area, it is possible to calculate the ice volume in a given region and its temporal variability, essential information to evaluate the impact of climate changes in the cryosphere.

The most accurate information on the SIT comes from surface drilling at different sites (Allison & Worby 1994), airborne electromagnetic induction techniques (Haas et al. 2009), and surface and ship-based observations (Worby et al. 2008). Surface perforation is more accurate but time-consuming and costly. The SIT can also be determined using laser-based altimeters in orbital satellites. In this case, the measured freeboard (ice plus snow) can be converted into the SIT through methods requiring information on the depth of the snow layer. The latter is obtained through passive remote sensors and other data such as sea ice density, water, and snow (Zwally et al. 2008, Yi et al. 2011). Other orbital satellites allow obtaining the main sea ice parameters such as extension, concentration,

and thickness remotely, but on a large temporal and regional scale. Among the alternatives is the use of passive remote sensors such as the Scanning Multichannel Microwave Radiometer (SMMR) of the Nimbus-7 satellite, the Special Sensor Microwave Imager (SSM/I), and the Special Sensor Microwave Imager/Sounder (SSMIS), a payload of the Defense Meteorological Satellite Program (DMSP) satellites, or active remote sensors such as synthetic aperture radar (SAR) (Aulicino et al. 2013).

The initial studies conducted by Tateyama et al. (2002) utilized multiple linear regression (MLR) between SIT and brightness temperature (T_b) from SSM/I sensors to distinguish various types of sea ice, such as new ice, young ice, and first-year ice. This preliminary study employed the PR19 (polarization ratio at a frequency of 19 GHz in both vertical and horizontal polarization) and the $R_{37V/85V}$ (ratio at frequencies of 37 GHz and 85 GHz in vertical polarization). They found a good correlation of up to $R = 0.81$ for thicknesses up to 0.8 m, limited by in-situ sampling. Martin et al. (2004) calculated the thin ice thickness (0–0.2 m) and the energy balance in Arctic polynyas using SSM/I sensor data carried by DMSP satellites. This analysis is extended by Naoki et al. (2008), who demonstrated a reasonably accurate estimate relating the brightness temperature (T_b) to the SIT in thin sea ice. In recent research, Chi & Kim (2021) analyzed the T_b data of all channels and polarizations provided by Advanced Microwave Scanning Radiometer-2 (AMSR2) sensor to estimate the thickness of sea ice in all typologies in the Arctic Ocean, identifying that the lowest frequencies (10.65–36.5 GHz) have the highest contribution in the models.

In Antarctica, specifically for the Weddell and Ross seas, Aulicino et al. (2013) have estimated the SIT by applying a series of filters to delimit open water, sea ice, and snow sites and, subsequently, used an algorithm that combines the difference and proportion of T_b polarization and thickness values for seasonal sea ice, up to a thickness of approximately 0.9 m in freezing conditions. The discussion on mapping greater thicknesses of sea ice from the gradient rate (GR) of vertically polarized T_b at 18 and 36 GHz was presented by Yoshizawa et al. (2018) for the Arctic Ocean with the AMSR2 sensor, applying the MLR to obtain the thickness of the level first-year ice (up to 2 m), with an accuracy of up to 0.10 m. Once the T_b increases with ice growth between new ice and first-year ice and decreases with the development of ice beyond the first-year ice (Wensnahan et al. 1993, Cavalieri 1994, Nakayama et al. 2000, Tateyama et al. 2002), the application of the MLR was restricted to the estimation of the SIT for the first-year ice.

It is important to analyze new methodologies through remote sensing to map sea ice concentration (SIC) and SIT in the Weddell Sea, an environment sensitive to climate change. Swathi et al. (2023) observed that the sea ice extent (SIE) of this sector has an insignificant negative relationship between the Indian Ocean Dipole (IOD) and the Southern Annular Mode (SAM), but a significantly positive relationship between the El Niño Southern Oscillation (ENSO) and the Pacific Oscillation (IPO). This resulted in an annual rate of SIE expansion of $2.63 \pm 3.2 \times 10^3 \text{ km}^2 \text{ year}^{-1}$ between 1979–2020. Regarding volume, there is also an increasing trend due to the thickening of sea ice in certain regions, but it is not statistically significant as the interannual variability is very large in this sector (Massonnet et al. 2013).

This investigation aims to estimate the SIT < 1.5 m in pixels with SIC \geq 90%, using T_b data obtained by an SSM/I passive microwave sensor, applying the spectral linear mixing model (SLMM) to estimate the SIC and the MLR to estimate the SIT. Our study was carried out for the Weddell Sea region, between austral autumns and winters.

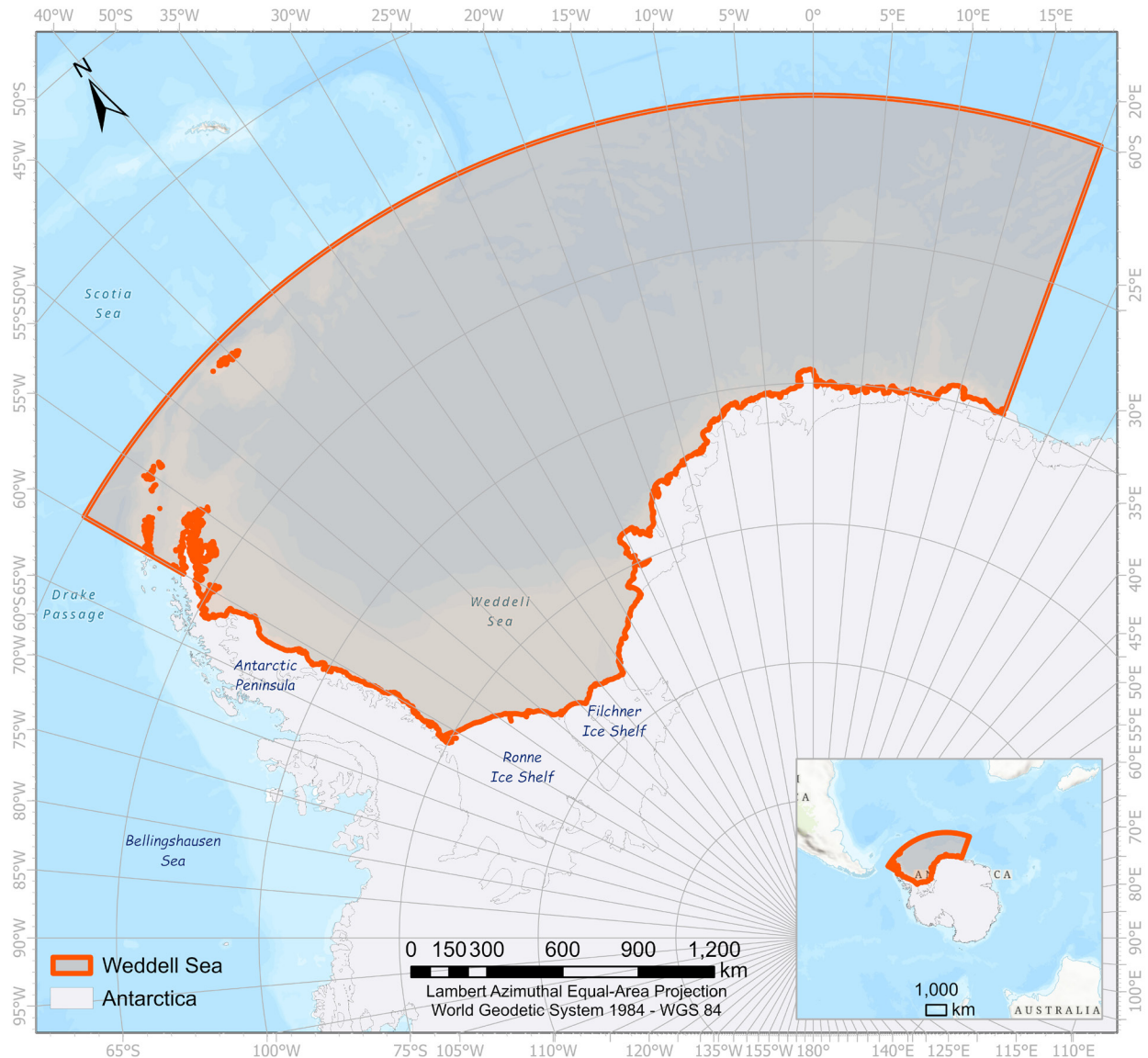


Figure 1. Delimitation of the Weddell Sea sector.

STUDY AREA AND DATA

Study area

The Southern Ocean, the water mass surrounding the Antarctic Continent, is not a formal geographical area delimited by continental landmasses regions like the Pacific, Atlantic, or Indian oceans. The strong Antarctic Circumpolar Current (ACC) flows clockwise continuously surrounding Antarctica, dominating the large-scale circulation of the Southern Ocean. The Antarctic coastline to the south of ACC includes two major indentations, the Weddell and the Ross seas (Talley et al. 2011).

The Weddell Sea is limited to the east by Queen Maud’s Land, the west by the Antarctic Peninsula, and the north by the Scotia Sea and ACC (Johnson et al. 1981). In general, its continental shelf is wide (up to 500 km) and deep (up to 600 m), but on its east side, the continental shelf is short (10 to 90 km)

and shallower (400 m), Fig. 1 shows its geographical limits (Zwally et al. 2002a, Parkinson & Cavalieri 2012, Parkinson 2019).

The Weddell Sea hosts a subpolar gyre (Treshnikov 1964), the Weddell Gyre, bringing deep, circumpolar, relatively warm and salt water to the south toward the Antarctic continent. It transports cooler and freshwater to the north in the deep waters of the Weddell Sea and as surface water. The circulation of this water is one of the main processes relevant to the climate in the Southern Hemisphere, affecting the ocean, atmosphere, and cryosphere. Another essential property of the Weddell Sea is the change in the intensity of recirculation, for example, the transport of shallow surface water bodies to the areas of newly formed water and bodies leaving the Antarctic system to the global ocean (Turner et al. 2009). However, climate change may affect this behavior, as reported by Strass et al. (2020). They conducted temperature sampling at the same locations, covering the entire water column to the bottom of the Weddell Sea between 1989–2019. This study identified widespread warming with similar long-term temperature trends below 700 m of depth, where the average rate of warming exceeded that of the global ocean by a factor of 5.

Passive remote sensors

For mapping the SIC and the SIT, it was used a time series of T_b images obtained by the SSM/I sensor of the DMSP F11 and F13 satellites, with 25 km spatial resolution and daily temporal resolution, covering the austral falls (March to May) and winters (June to August) (Turner et al. 2020) from 1992–2009. Our analyzed period did not include the austral spring and summer months, as the SLMM (model for SIC) and the MLR (model for SIT) are not adjusted when the sea ice is in the process of thawing. Furthermore, the month of September was also not analyzed, as there were not enough field data available by Antarctic Sea Ice Processes and Climate (ASPeCt) to carry out the sampling and validation of the applied models.

For these images from passive remote sensors, radiometric corrections of these data sets are necessary before they can be used, as they come from satellites with different altitudes, orbits, and angles of incidence (Cavalieri et al. 1999). Therefore, we used intercalibrated T_b data between SSM/I radiometers from the Fundamental Climate Data Record (FCDR), available at <https://n5eil01u.ecs.nsidc.org/MEASURES/NSIDC-0630.001/>. All SSM/I passive remote sensor channels are intercalibrated to sensor F13, chosen as the reference sensor due to its long life, stable calibration, and minimal change in equatorial crossing time due to orbit deviation (Berg et al. 2018).

For the validation of the SIC mapping calculated on the SSM/I sensor data, SIC data (spatial resolution 6.25 km x 6.25 km) from the ARTIST Sea Ice (ASI) algorithm was applied to the Advanced Microwave Scanning Radiometer for Earth Observing System (AMSR-E) sensor (Spren et al. 2008), provided by Universität Bremen, were used on coincident dates in the freezing period. The spatial resolution of the SSM/I sensor images was matched with the nearest neighborhood resampling was performed to generate resampled images with pixel spatial resolution at 25 km x 25 km.

Antarctic Sea Ice Processes and Climate program (ASPeCt) local sea ice thickness (SIT) data

In 1997, the Scientific Committee for Antarctic Research (SCAR) established the ASPeCt program with the initial objective of compiling the records related to sea ice observations made on ships in Antarctica into a single database. This included the total ice concentration and estimates of areal

coverage, thickness, floe size, topography, and snow cover. In the visual observations of the SIT made available by ASPeCt program, they considered data collected within six nautical miles around the vessels in expeditions carried out between 1981–2005 (Worby & Allison 1999). The SIT estimation error for new ice (< 0.1 m thick) is $\pm 50\%$, $\pm 30\%$, for ice thickness from 0.1 to 0.3 m, and $\pm 20\%$ for sea ice thickness > 0.3 m. These errors are independent estimates at each point and, therefore, are spatially related. For the SIC, estimated by tenths, the accuracy is $\pm 10\%$, which applies to the total concentration and the partial concentrations of each type of ice (Worby et al. 2008). The ASPeCt program data underestimate the mean sea ice thickness because ships generally avoid thick sea ice (Shi et al. 2021).

At the passive sensor's spatial resolution (25 km x 25 km), it is possible to find several points with ship observations. Our research used all SIT data from ASPeCt program observations into the same grid cell of the SSM/I sensor. This approach considers the Aulicino et al. (2013) observation that applying Gaussian weighting to all ASPeCt program observations within the same grid cell results in a lower linear correlation (R) in the SIT estimation. Table I shows details of the ship trips in the Weddell Sea used in our study.

ICESat SIT data

The Ice, Cloud, and land Elevation Satellite (ICESat) consists of a precision laser altimeter system used to measure elevation points on the surface with 70 m footprints and spaced every 172 m along

Table I. Ship trips with local SIT observations obtained by the ASPeCt program in the Weddell Sea.

Cruise	Period (MM/DD/AAAA)	Region	Expedition	Samples
Akademic Fedorov	04/19–04/21/1992	Lat: 67.2° S–70° S Long: 11.6° E–15.7° E	37th Russian expedition	47
Akademic Fedorov	05/02–06/17/1992	Lat: 58.7° S–67.6° S Long: 24.8° W–58.8° W	37th Russian exp (ISW)	658
Akademic Fedorov	03/10–04/14/1993	Lat: 68° S–70° S Long: 10.3° E–18.2° E	38th Russian expedition	52
Mikhail Somov	03/08–05/03/1994	Lat: 61.8° S–70° S Long: 14.9° E–25.2° W	39th Russian expedition	155
Nathaniel B. Palmer	07/13–08/15/1994	Lat: 57.4° S–67.9° S Long: 3.9° E–21.5° W	NBP 94-4 (ANZFLUX)	163
Akademic Fedorov	03/11–03/14/1995	Lat: 69.2° S–70° S Long: 11.6° E–13° E	40th Russian expedition	11
Akademic Fedorov	04/10–04/14/1995	Lat: 67.2° S–70° S Long: 10.3° E–13.9° E	40th Russian expedition	68
Akademic Fedorov	05/29–06/07/1996	Lat: 59.9° S–70° S Long: 19.9° E–29.6° W	41st Russian expedition	98
Akademic Fedorov	05/21–07/22/1997	Lat: 61.5° S–70° S Long: 10.4° E–19.6° E	42nd Russian expedition	121
Akademic Fedorov	05/29–06/03/1998	Lat: 64.7° S–70° S Long: 11.2° E–20° E	43rd Russian expedition	57
Polarstern	03/10–03/14/2005	Lat: 63.5° S–64.5° S Long: 45.3° W–52.1° W	ANT XXII/3	19
Nathaniel B. Palmer	07/29–09/06/2005	Lat: 56.9° S–65.8° S Long: 6.1° E–6.5° W	NBP 05-06 (MaudNESS)	228

Table II. SIT maps were obtained by ICESat observations in the Weddell Sea using the SICCI methods.

Year	Autumn (MA)	Winter (MJ)
2004	---	18 May–21 June (MJ04)
2005	---	20 May–23 June (MJ05)
2006	---	24 May–26 June (MJ06)
2007	12 March–14 April (MA07)	---

track a (Zwally et al. 2002b) with two channels at 1064 nm and 532 nm, allowing to detect the distance between the snow surface and the sea surface, called total freeboard, and from these data apply algorithms for SIT retrieval (Kwok et al. 2004).

In a study on the SIT mapping in the Weddell Sea, developed by Kern et al. (2016), the approach developed by the Sea Ice Climate Change Initiative (SICCI) project of the European Space Agency (ESA) was applied to ICESat data, with a grid resolution of 100 km that is considered a data mean over long periods (5–33 days) to obtain dense coverage of valid data, the autumn (March–April) and winter (May–June) periods are used in this study, according to Table II. In this SICCI approach, the total freeboard and snow depth measured by the AMSR-E was considered, considering the densities of open water: $\rho_{\text{water}} = 1,023.9 \text{ kg m}^{-3}$, snow: $\rho_{\text{snow}} = 300.0 \text{ kg m}^{-3}$, and sea ice: $\rho_{\text{sea ice}} = 915.1 \text{ kg m}^{-3}$.

One of the primary uncertainty sources in the SIT estimation by SICCI is high snow accumulation over the Antarctic sea ice. This snow load depresses the thinner ice surface, lowering the surface and allowing seawater to infiltrate the base of the snow layer, leading to the formation of snow ice when the resulting slush freezes (Massom et al. 2001). Suppose the SICCI considers the same snow depth and freeboard values, with a 5 cm snow depth error (expected from deep snow recovery of passive microwaves). In that case, we will find an error greater than 0.37 m in the SIT estimate from the ICESat data (Kurtz & Markus 2012).

MATERIALS AND METHODS

Fig. 2 shows the flow chart used in this research to estimate the SIT < 1.5 m pixels with SIC \geq 90% in the Weddell Sea from T_b images derived by SSM/I sensors. Methodological details are addressed below.

Mapping of the sea ice concentration (SIC) using the spectral linear mixing model (SLMM)

The brightness recorded on satellite images is an integrated sum of the brightness of all targets within the sensor's Instant Field of View (IFOV). Thus, the detected brightness results from mixing different materials within the image pixels (Shimabukuro & Smith 1991). Spectral mixing is a procedure by which the measured spectrum of a pixel is decomposed into a collection of constituent spectra or final members (Keshava 2003). For this procedure, it is necessary to obtain the spectral signature values of the targets, which may be through spectral libraries, spectral analysis of samples of each component in the laboratory, or selecting pixels in an image considered pure (Schowengerdt 2006).

In our research, a SLMM was applied to delimit the pixels in the SSM/I passive remote sensor T_b images with SIC \geq 90%, allowing in sequence to analyze the MLR to estimate the SIT in the time series.

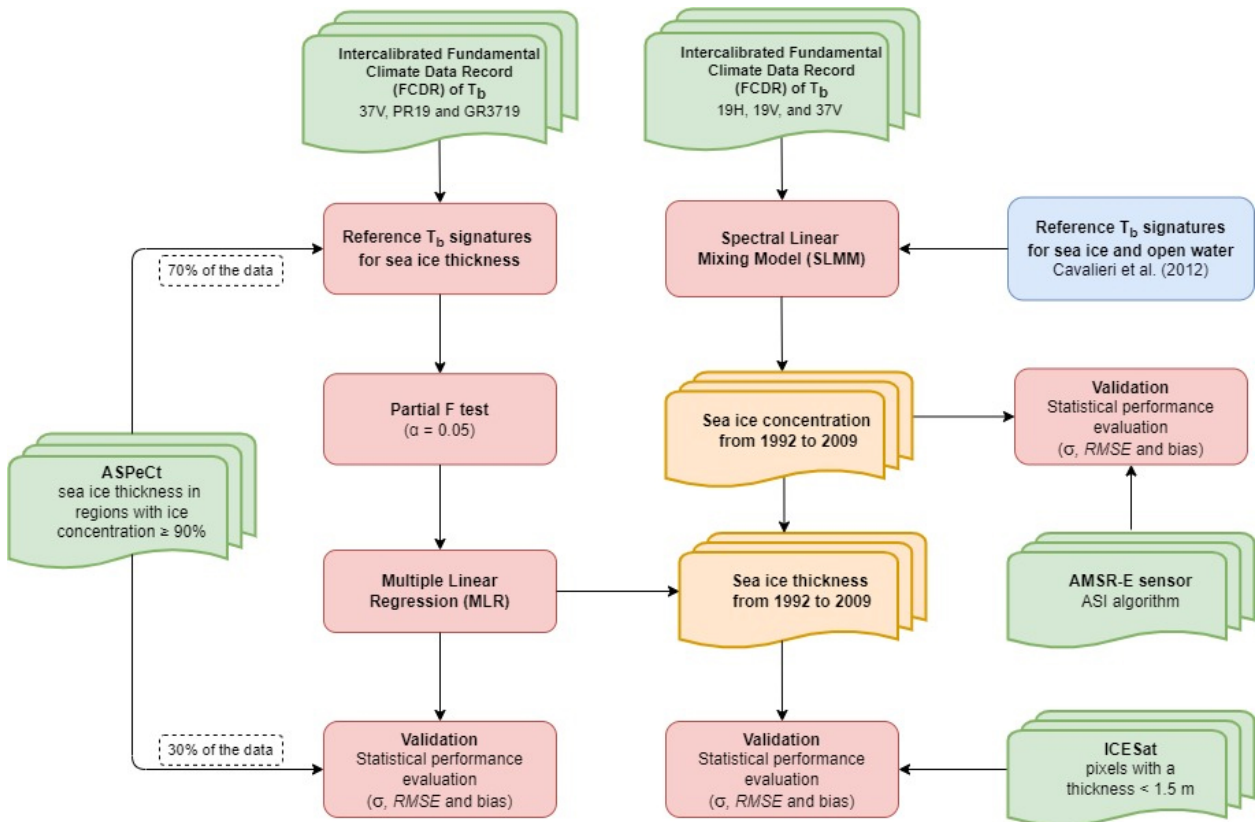


Figure 2. The methodology applied to estimate the SIT < 1.5 m in pixels with SIC ≥ 90% in the Weddell Sea using T_b images derived by the SSM/I sensor.

We propose the application of the SLMM since Hillebrand et al. (2022) obtained a difference of 1.4% and a standard deviation (σ) of 13.6%. Root mean square error (RMSE) of 15.3% when comparing the SIC obtained through passive (SSM/I) and active (Sentinel 1A) sensors in the oceanic region located west of the Peninsula Antarctica. In the SLMM, we consider only channels and polarizations 19H, 19V, and 37V since they show open water with T_b signatures in contrast with sea ice (Meier & Markus 2015). We consider the reference T_b signatures for sea ice and open water calibrated to the F13 satellite SSM/I passive sensor, emitted during winter in the Southern Ocean, presented by Cavaliere et al. (2012).

The SLMM assumes that each pixel’s response (T_b) in a given passive sensor channel results from a linear combination of each end member in the IFOV and is represented in grid resolution (Freitas et al. 2018). The contribution of each final member is weighted by the fraction of this component in each pixel, represented by equation 1 (Adams et al. 1995, Haertel & Shimabukuro 2005, Quintano et al. 2012):

$$R_k = \sum_{j=1}^m r_{j,k} f_j + v_k, \quad k = 1, \dots, p \tag{1}$$

where R_k is the average spectral reflectance of the pixel in the k spectral band, $r_{j,k}$ the spectral reflectance of j component in k spectral band, f_j the proportion of j component within the pixel, m the number of components, v_k the residual error for k spectral band, and p the number of spectral bands.

Usually, the number of spectral bands p is greater than the number of unknowns m , resulting in a system of linear equations where the number of equations is greater than the number of unknowns (Freitas et al. 2018). A system with these characteristics does not have an exact solution, and an approximation satisfying a given criterion is generally adopted. Consequently, our research used the SLMM’s method of least squares with a restriction, which consists of estimating each component’s proportion within the pixel, minimizing the sum of errors to the square. The proportion values obtained by this algorithm result in non-negative numbers (physical meaning) and the sum equal to 1 (Shimabukuro et al. 2020), according to the two restrictions proposed in equations 2 and 3:

$$\sum_{j=1}^m f_j = 1 \tag{2}$$

$$f_j \geq 0 \tag{3}$$

According to the SLMM assumptions, a set of n linear equations can be established for each pixel in each spectral band. Thus, equation 4 shows that for each i pixel in k spectral band, we will find a residual value (Haertel & Shimabukuro 2005):

$$v_{i,k} = R_{i,k} - \sum_{j=1}^m f_{ij} r_{j,k} \tag{4}$$

where $R_{i,k}$ is the mean spectral reflectance in i pixel in k spectral band, f_{ij} is the proportion of the i pixel covered by the j component, $r_{j,k}$ the spectral reflectance unknown for j component in k spectral band, $v_{i,k}$ The residual in i pixel in k spectral band, m the number of components, n the number of pixels used, and p the number of spectral bands of the images.

By obtaining the residual values per pixel, the mean error per band and total one can be calculated by spatializing through images the distribution of the error using this matrix notation (5):

$$E_k = R_k - F \cdot r_k \tag{5}$$

where E_k is the n -dimensional vector of the residues in k -spectral band, R_k the n -dimensional vector of the spectral response of the pixels in k -spectral band, F the $n \times m$ matrix of the proportions, and r_k the m -dimensional vector of spectral response of components in k -spectral band.

Other restrictions Shimabukuro & Smith (1991) reported are the number of pixels $n > m$ and that $m \leq p + 1$, so the linear equation system has a solution. The design of equations is solved by minimum squares adjusting, whose objective is to estimate f_j , minimizing the sum of the squares of errors $v_{i,k}$, subject to restrictions 2 and 3.

The solution by the method of least squares for unknown spectral reflectances can be calculated by equation 6 (Haertel & Shimabukuro 2005):

$$r_k = (F^T F)^{-1} F^T R_k \tag{6}$$

where r_k is the m -dimensional vector of the spectral response of the components in k -band, F the $n \times m$ matrix of the proportions, F^T the $n \times m$ matrix of the proportions, and R_k the n -dimensional vector of the spectral response of the pixels in k -band spectral.

SIT estimate using multiple linear regression (MLR)

In this step, the intercalibrated T_b of the SSM/I sensor of the channel and polarization 37V and the ratios GR3719 (equation 7) and PR19 (equation 8) were obtained for the different SIT < 1.5 m provided by the ASPeCt program for the Weddell Sea area (Table I). The 85 GHz frequency was not considered because it suffers atmospheric interference in its signal, requiring complementary corrections (Yoshizawa et al. 2018). Also, higher frequencies have a lower depth of penetration into the sea ice compared to lower frequencies, such as 19 GHz and 37 GHz (Yoshizawa et al. 2018; Chi & Kim 2021).

$$GR3719 = \frac{T_b(37V) - T_b(19V)}{T_b(37V) + T_b(19V)} \quad (7)$$

$$PR19 = \frac{T_b(19V) - T_b(19H)}{T_b(19V) + T_b(19H)} \quad (8)$$

where $GR3719$ is the gradient ratio at the frequency of 37 GHz in vertical polarization and 19 GHz in vertical polarization, $PR19$ is the polarization ratio at the frequency of 19 GHz in vertical and horizontal polarization, $T_b(19V)$ the brightness temperature at the 19 GHz frequency in vertical polarization, $T_b(19H)$ the brightness temperature at the 19 GHz frequency in horizontal polarization, and $T_b(37V)$ the brightness temperature at the 37 GHz frequency in vertical polarization.

Since MLR is a parametric statistic, a test to verify the data normality was previously performed. For this, the Shapiro-Wilk test was applied, which consists of a non-parametric evaluation, ideal for evaluating different distributions and sizes of samples (Shapiro & Wilk 1965). A p -value < 0.05 to consider whether the distribution was normal or not.

After confirming the normal distribution of the 1,520 sample points obtained in the ASPeCt program, 70% of these points were randomly separated to generate the MLR and 30% to carry out the validation with the application of statistical indicators: σ , $RMSE$, and bias (Beitsch et al. 2015). In the data that were used to generate the MLR, the partial F test was then applied to identify the linear relationship between the dependent variable and each independent variable, thus allowing the identification of independent variables that can be eliminated from the model owing to their lack of statistical relationship at the established level of significance (p -value < 0.05). Once the statistically significant independent variables were identified, the regression model was generated according to equation 9. For the structuring of MLR (Hair et al. 1998), the SIT obtained through ASPeCt program local observations was considered the dependent variable, and the values of the statistically significant parameters were obtained by the SSM/I sensor as independent variables.

$$y = \beta_0 + \beta_1 x_1 + \beta_2 x_2 + \dots + \beta_k x_k + \varepsilon \quad (9)$$

where y is the dependent variable, x_1 to x_k the independent variables, β_0 the intercept for y , β_1 to β_k the slope coefficients between y about the x_1 to x_k variables, and ε random error, including other factors that may influence the response of the variable y , except for regression variables x_1 to x_k .

Validation in the SIC estimates obtained by the SLMM and the SIT calculated by the MLR in the Weddell Sea

For the validation of the temporal mapping of the SIC obtained by the SLMM in the SSM/I data, a statistical analysis will be performed comparing with the SIC obtained by the ASI algorithm in the

AMSR-E sensor on coincident dates during the freezing period in 2008–2009. To validate the MLR in the temporal mapping of the SIT estimate, we used in the analysis an independent SIT dataset provided by the ICESat satellite (Table II) through the SICCI approach (Kern et al. 2016) considering only samples with SIT < 1.5 m. The statistical indicators σ , *RMSE*, and bias (Beitsch et al. 2015) are applied for SIC and SIT.

RESULTS

MLR coefficients and validation of the SIT estimation

The partial *F* test, with a significance interval *p*-value < 0.05, was applied to 70% of the SIT local observations at random (SIT < 1.5 m) was obtained by the ASPeCt program about parameters 37V, GR3719, and PR19 obtained by the SSM/I sensor. We identified that statistically, the parameters 37V and GR3719 should be considered independent variables in the MLR. These results follow the research carried out by Yoshizawa et al. (2018), noting that the spectral gradients of emissivities between 19 GHz and higher frequencies become accentuated with the increase of the flat draft of the first-year ice and, therefore, support that the GR values can be used to detect variations of the flat draft.

The MLR provides the coefficients to estimate the SIT (equation 10), limiting the sampling depth to 1.5 m as a function of the data available from the ASPeCt program and restricted to sites where SIC \geq 90%. In MLR modeling, we found $R^2 = 0.49$ and $\sigma = 0.26$ m, with the 1,063 observations used in modeling.

$$\text{SIT} = 2.529 - 0.009 (37V) - 8.803 (\text{GR3719}) \quad (10)$$

where SIT is the sea ice thickness (m) considered as the dependent variable, and the parameters 37V and GR3719 are the values of the independent variables.

To validate the MLR, performed a comparative analysis was between the SIT (30% of the samples) obtained through local observations in sites with SIC \geq 90% provided by the ASPeCt program about the SIT estimated by the MLR (equation 10) in these exact locations. Then, the statistical indicators σ , *RMSE* and bias were applied to the differences, obtaining the following results: 0.247 m, 0.268 m, and 0.103 m.

A simple linear regression was applied using local observations to identify whether the surface snow layer would affect the 37V and GR3719 values of the passive sensor SSM/I, finding at the end, respectively, $R^2 = 0.012$ and $R^2 = 0.056$.

Validation of mapping on SIC estimates obtained by SLMM and SIT calculated by MLR in the Weddell Sea

Results of σ , *RMSE*, and bias statistical analyzes to validate the difference between the temporal mapping of the SIC obtained by the SLMM in the SSM/I sensor data to that obtained by the ASI algorithm in the AMSR-E sensor and also to validate the difference between the temporal mapping of the SIT (< 1.5m) estimated by the MLR in the images of the passive sensor SSM/I with that estimated by the SICCI in the ICESat satellite data (Kern et al. 2016), are shown in Tables III and IV, respectively.

Table III. σ , *RMSE*, and bias of the SIC differences calculated by the SLMM method in SSM/I sensor images with the SIC calculated by the ASI method in the AMSR-E sensor images in the Weddell Sea during the freezing period.

Date (mm/dd/yyyy)	σ (%)	<i>RMSE</i> (%)	Bias (%)
03/01/2008	13.1	13.2	-1.2
03/15/2008	13.7	13.9	-1.8
04/01/2008	12.2	12.3	-1.8
04/15/2008	10.4	11.0	-3.5
05/01/2008	10.8	11.2	-3.1
05/15/2008	10.6	10.9	-2.4
06/01/2008	11.1	12.4	-5.4
06/15/2008	9.1	10.6	-5.3
07/01/2008	9.2	10.0	-3.8
07/15/2008	8.6	10.1	-5.3
08/01/2008	8.0	9.0	-4.1
08/15/2008	8.8	9.1	-2.3
03/01/2009	11.4	11.4	-0.6
03/15/2009	12.3	12.3	0.7
04/01/2009	10.7	10.7	0.3
04/15/2009	10.2	10.2	-0.8
05/01/2009	10.5	10.7	-2.1
05/15/2009	9.7	9.9	-2.1
06/01/2009	10.6	11.0	-2.9
06/15/2009	9.6	10.7	-4.8
07/01/2009	8.0	8.4	-2.6
07/15/2009	8.2	8.6	-2.5
08/01/2009	17.9	19.0	-6.4
08/15/2009	7.1	7.8	-3.2
Mean	10.5	11.0	-2.8

Table IV. Summary of the statistical performance found between the difference of SIT obtained through the SICCI approach in the data from the ICESat satellite about the thickness estimated through the MLR in the images of the passive sensor SSM/I in the freezing period.

	Period*	σ (m)	<i>RMSE</i> (m)	Bias (m)
Autumn	MA07	0.293	0.318	-0.124
Winter	MJ04	0.439	0.460	0.138
	MJ05	0.419	0.421	0.044
	MJ06	0.465	0.484	0.137

* You can find the description of the abbreviation of the periods in Table II.

Multitemporal analysis of SIC and the SIT in SSM/I sensor images

The maps of the mean concentration (%) and thickness (m) of the sea ice in the Weddell Sea for each month (March to August) from 1992–2009 are available at <https://doi.org/10.7910/DVN/QA8XD3>. We can see from Fig. 3 that the highest concentrations of sea ice are found in the western part of the Weddell Sea in the autumn, advancing entirely into the region in the southern winter. Holland (2014) reported that the SIC trends are positive towards the eastern Weddell Sea, that is, mainly associated with the intensification of easterly winds. We can also observe a polynya off the Ronne-Filchner Ice Shelf, thus affecting the SIT estimate through MLR. The follow-up of this site is essential because the sea ice formation decline can increase the rates of basal melting and accelerate the mass loss of this century’s sea ice cover (Hattermann et al. 2021).

The advancement of the SIC increase towards the north and east of the Weddell Sea during winter is related to low wind speeds, and the westerly winds are considerably weakened south of 65°S (Kumar et al. 2021). Furthermore, the Weddell Gyre is relatively weak due to the meridional temperature difference, resulting in ocean heat divergence and sea ice retreat towards the north of 65°S (Lee et al. 2017).

The SIT values seasonal average maps for the Weddell Sea from 1992–2009, during the freezing period, are shown in Fig. 4. The thickest ice is found predominantly in the west part of the Weddell Sea,

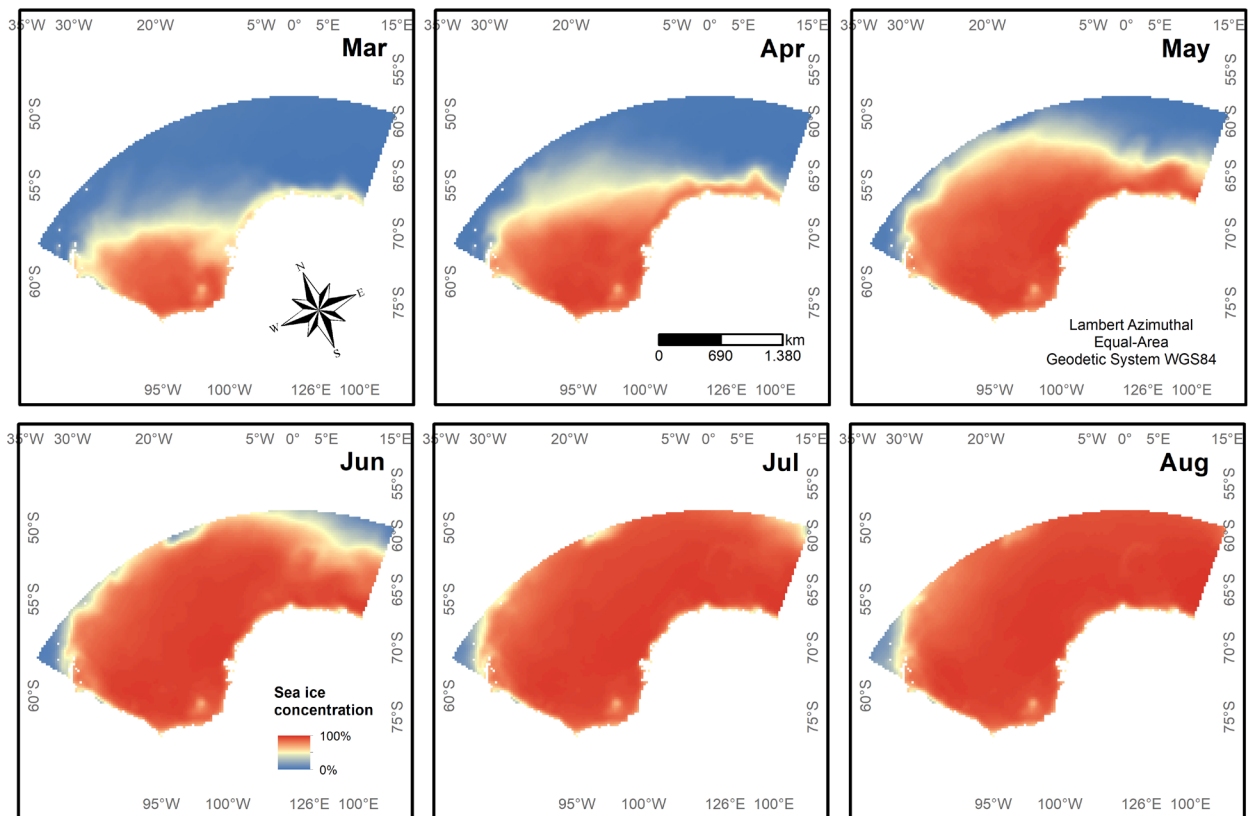


Figure 3. The SIC (%) monthly mean in the Weddell Sea for each month from 1992 to 2009, estimated from the SLMM applied to the T_b images of the passive remote sensor of SSM/I.

and the first-year ice areas advanced over the new ice (< 0.1 m) and young ice (0.1 to 0.3 m), reaching the most significant areas and thickest ice by the end of the southern winter. Several studies (Yi et al. 2011, Kern et al. 2016, Shi et al. 2021) point out that during the southern spring, the new and young ice increases its thickness and, consequently, increases the first-year ice cover in the Weddell Sea. As in our study, the ASPeCt program local SIT observations used to elaborate MLR cover only the autumn and southern winter periods. The model is not adjusted to perform mapping during the austral spring.

In addition, Fig. 4 shows that our model could map the polynya off the Ronne-Filchner ice shelf. Aulicino et al. (2013) have also successfully located this polynya through the SIT estimate maps on T_b images obtained by the SSM/I sensor between April and October.

Fig. 5 allows us to analyze the SIT ($m\ year^{-1}$) linear trend in the Weddell Sea for the 1992–2009 period obtained through the least squares regression method for each month. To the south of the Weddell Sea, we identified SIT thickening, a result also identified by Holland et al. (2014) who associated with a decrease in ice export to the north, away from the coast. They also pointed out that the loss of thermodynamic ice to the north may result from the decrease in the export of cold and dry air from Antarctica or, perhaps, a shift to the south of the warmer ACC waters, any of which can be caused by changes in winds. We highlight the clear interannual evolution of the SIT in the Ronne-Filchner ice shelf polynya, with a tendency to expand its limits throughout the austral autumn.

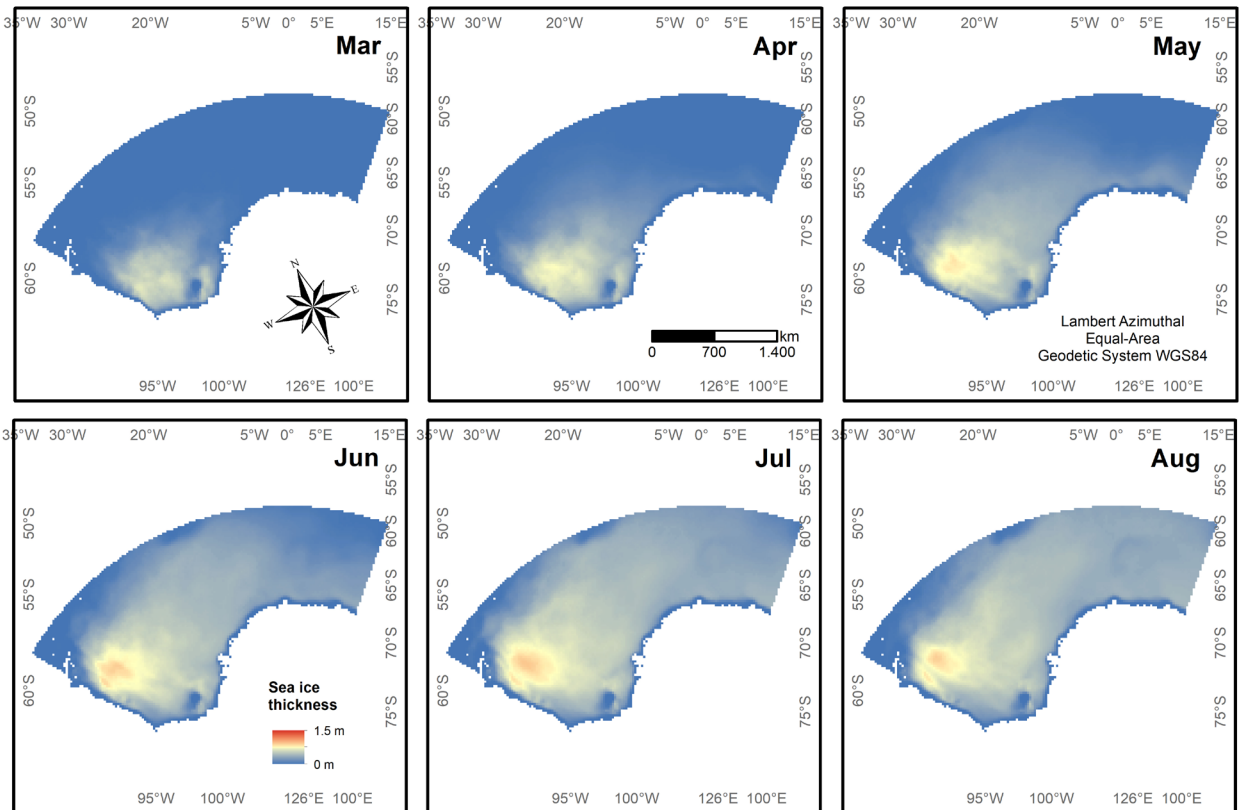


Figure 4. Monthly mean SIT (m) in the Weddell Sea from 1992 to 2009, estimated from the MLR applied to the SSM/I passive remote sensor images.

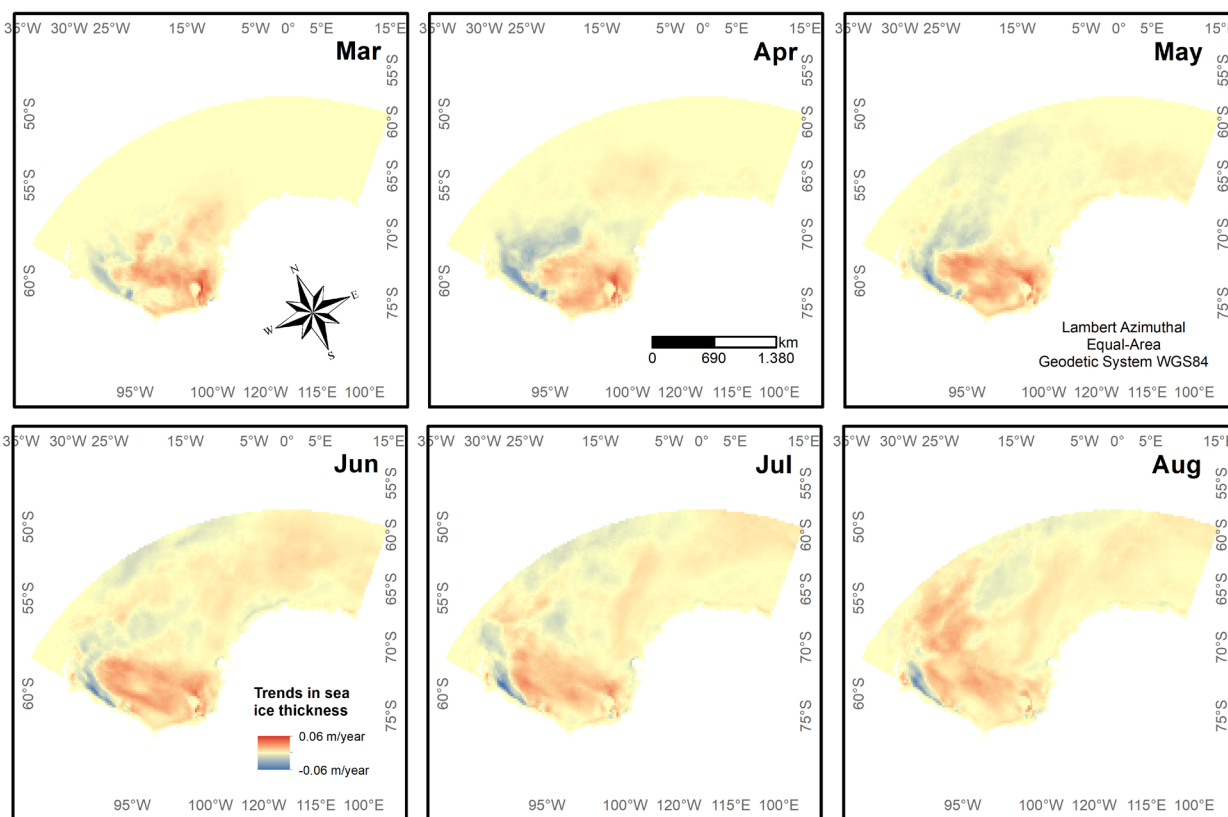


Figure 5. Monthly SIT trend (m year^{-1}) in the Weddell Sea from 1992 to 2009, estimated from the MLR applied to the SSM/I passive remote sensor images.

On the east coast of the Antarctic Peninsula, although we found the largest SIT, a decreasing trend of the SIT was observed in the 1992–2009 period, a worrying result for this region, as offshore ice shelves play a crucial role in driving the global ocean conveyor belt as a large Antarctic Bottom Water formation site (Orsi et al. 2002).

DISCUSSION

Kern & Spreen (2015) applied an alternative approach to SICCI using ICESat data to estimate the SIT in the Weddell Sea; they assumed that the freeboard of the sea ice is zero and that the total freeboard is equal to the depth of the snow. They found a mean SIT uncertainty of 0.72 ± 0.09 m, which is close to $\sim 40\%$ of the mean SIT value of 1.73 ± 0.38 m, and in the winter, the relative uncertainty is up to $\sim 50\%$. Our study found a relative uncertainty of $\sim 19\%$ in the southern winter to estimate the SIT (up to 1.5 m thick), comparing the ASPECT program local observation data used for validation against the SIT calculated by the MLR. These uncertainties affect the calculation of ice thickness and volume estimates, masking the determination of long-term trends or cyclic variabilities in the sea ice cover. Kurtz & Markus (2012) found that stretching the observations time series, together with a better determination of the interannual variability of the densities of sea ice and snow, would allow a statistically significant long-term SIT and ice volume trends determination in the Southern Ocean.

The SIT sub-estimation in the Weddell Sea area based on the MLR applied to SSM/I passive remote sensor images (Table III) was also observed by Shi et al. (2021) when using four review models, German Estimating the Circulation and Climate of the Ocean Version 2 (GECCO2), Southern Ocean State Estimate (SOSE), Nucleus for European Modelling of the Ocean (NEMO) e o Global Ice-Ocean Modeling and Assimilation System (GIOMAS) to estimate the SIT and compare it with ICESat data, finding an average error ranging from -0.52 m (GIOMAS) to -0.99 m (SOSE) and *RMSE* values ranging from 0.44 m (NEMO) to 0.68 m (GIOMAS).

During the winter, we found that sea ice became thicker (from 0.5 to 1.25 m) in the Weddell Sea central area; the thickest ice is located on the east coast of the Antarctic Peninsula. Kern et al. (2016) found the same behavior using ICESat data, with the SIT ranging from 0.5 to 1.5 m thick in winter. In the winter-spring transition, the ice thickness increases to the west of the Weddell Sea, while the thinner sea ice (< 1 m) is concentrated in the central region (Kern et al. 2016, Yi et al. 2011). Kurtz & Markus (2012) also found that the thickest sea ice is on the west coast of the Weddell Sea, but in this sector, the SIT trend gets thinner (0.07 m year⁻¹). The SIT was also thinner (-0.04 m year⁻¹) from 2003 to 2008, but this is probably due to the interannual density variability of snow and sea ice cover. Our study also found that the Weddell Sea west coast shows the highest reduction trend in the SIT (-0.06 m year⁻¹), mainly in the southern autumn period; however, in the same period, we observed the highest increase in ice thickness (0.06 m year⁻¹) recorded at the borders of the Ronne-Filchner polynya. One factor affecting the formation of sea ice in this region polynyas (off the ice shelf front) is the cold and dry winds blowing from the continent (Paul et al. 2015). As the water freezes, the rejection of brine forms high salinity shelf water (HSSW) that forces a thermohaline circulation below the ice shelf advancing to the south direction. As a result of the pressure dependence of the melting point of the ice, HSSW cooling at freezing temperatures on the surface may lead to basal melting over the deeper parts of the ice shelf (Hattermann et al. 2021).

Renner & Lytle (2007) evaluated the SIT using data from 14 Upward-looking Sonars (ULS) anchored along two transects during 1990–1994 and 1996–1998 in the Weddell Sea. The thickest ice is observed on the continental slope near the Antarctic Peninsula's northern tip and the Weddell Sea's east coast. In these regions, the high ice drift velocity, high concentrations of ice, and the coast's proximity increase the formation of ridges, resulting in greater ice thicknesses. However, thin ice was found in the northern part of the Weddell Sea along Greenwich Meridian (0°), where concentrations are lower. In the central part of this Sea, ice drifting is slow because it is located at the center of the Weddell Gyre.

CONCLUSIONS

In this study, we considered the T_b of the channel and polarization 37V and the GR3719 gradient ratio obtained from SSM/I passive sensor images to develop an MLR capable of estimating seasonal SIT at a maximum thickness of 1.5 m. The MLR modeling was based on SIT data obtained from ships' observations (from the ASPeCt program) in locations with SIC \geq 90%, with 70% of the samples being randomly separated for the elaboration of the model and 30% for validation. From this validated MLR, the temporal mapping of SIT < 1.5 m in pixels with SIC \geq 90% located by the SLMM applied to channels and polarizations 19H, 19V, and 37V were performed. These SIT mappings undergo a second validation with the laser altimeter data (ICESat) calculated by the SICCI method.

In the MLR modeling to estimate the SIT < 1.5 m, we found in the validation $R^2 = 0.57$, $RMSE = 0.268$ m, and bias of 0.103 m. When comparing the SIT mappings obtained by applying the MLR to the SMM/I data in relation to the ICESat (pixels with a thickness < 1.5 m), we identified an $RMSE$ ranging between 0.318 m to 0.484 m and bias ranging from -0.124 m to 0.138 m. The methods proposed in this article allow retrieving information on the temporal evolution of SIC, SIT and SIT trends in the Weddell Sea during southern autumn and winter. We do not recommend applying this method to study spring and summer sea ice, as the SLMM and MLR are not adjusted for thawing periods. One reason is the melting of snow on the sea ice surface, which can affect the salinity of the interface, compromising the salinity profile of the upper layer of sea ice and its emissivity response.

Acknowledgments

This research paper was supported by the Conselho Nacional de Desenvolvimento Científico e Tecnológico - CNPq (Process 465680/2014-3- NCT da Criosfera) and financed by the Research Support Foundation of the State of Rio Grande do Sul (FAPERGS) projects numbers 17/2551-0000518-0 and 21/2551-0002042-3.

The main author would like to express gratitude to Prof. Dr. Christian Haas, a researcher at the Alfred Wegener Institute for Polar and Marine Research (AWI), for his contributions to this research and for providing guidance during the scientific exchange held at the institution in February 2022. We would also like to thank the Scientific Committee on Antarctic Research (SCAR) for providing financial support through the SCAR Fellowship Programme 2021. Funding went towards the project entitled “Spectral linear mixing model applied to data from passive microwave radiometers for sea ice thickness mapping in the Weddell Sea “ and enabled the main author’s exchange at AWI.

No potential conflict of interest was reported by the author(s).

REFERENCES

- ADAMS JB, SABOL D, KAPOV V, ALMEIDA R, ROBERTS A, SMITH MO & GILLESPIE AR. 1995. Classification of multispectral images based on fractions of endmembers: application to land-cover change in the Brazilian Amazon. *Remote Sens Environ* 52: 137-154.
- ALLISON I & WORBY AP. 1994. Seasonal changes of sea-ice characteristics off East Antarctica. *Ann Glaciol* 20: 195-201.
- AULICINO G, FUSCO G, KERN S & BUDILLON G. 2013. Estimation of sea-ice thickness in Ross and Weddell Seas from SSM/I brightness temperatures. *IEEE Trans Geosci Remote Sens* 52: 4122-4140.
- BEITSCH A, KERN S & KALESCHKE L. 2015. Comparison of SSM/I and AMSR-E Sea Ice Concentrations with ASPeCt Ship Observations Around Antarctica. *IEEE Trans Geosci Remote Sens* 43: 1985-1996.
- BERG W, KROODSMA R, KUMMEROW CD & MCKAGUE DS. 2018. Fundamental Climate Data Records of Microwave Brightness Temperatures. *Remote Sens* 10: 1306.
- CAVALIERI DJ. 1994. A microwave technique for mapping thin ice. *J Geophys Res Oceans* 99: 12561-12572.
- CAVALIERI DJ, PARKINSON CL, DIGIROLAMO N & IVANOFF A. 2012. Intersensor Calibration Between F13 SSM/I and F17 SSMIS for Global Sea Ice Data Records. *IEEE Geosci Remote Sens Lett* 9: 233-236.
- CAVALIERI DJ, PARKINSON CL, GLOERSEN P, COMISO JC & ZWALLY HJ. 1999. Deriving long-term time series of sea ice cover from satellite passive-microwave multisensor data sets. *J Geophys Res-Oceans* 104: 15803-15814.
- CHI J & KIM HC. 2021. Retrieval of daily sea ice thickness from AMSR2 passive microwave data using ensemble convolutional neural networks. *GISci Remote Sens* 58: 812-830.
- FREITAS MW DE, MENDES JÚNIOR CW, ARIGONY-NETO J, COSTI J & SIMÕES JC. 2018. A multiscale subpixel mixture analysis applied for melt detection using passive microwave and radar scatterometer image time series of the Antarctic Peninsula (1999-2009). *Ann Glaciol* 59: 16-28.
- HAAS C, LOBACH J, HENDRICKS S, RABENSTEIN L & PFAFFLING A. 2009. Helicopter-borne measurements of sea ice thickness, using a small and lightweight digital EM system. *J Appl Geophys* 67: 234-241.

- HAERTEL VF & SHIMABUKURO YE. 2005. Spectral linear mixing model in low spatial resolution image data. *IEEE Trans Geosci Remote Sens* 43: 2555-2562.
- HAIR JR, BLACK WC, BABIN BJ, ANDERSON RE & TATHAM RL. 1998. *Multivariate data analysis*. Upper Saddle River: Prentice-Hall.
- HATTERMANN T, NICHOLLS KW, HELLMER HH, DAVIS PE, JANOUT MA, ØSTERHUS S, SCHLOSSER E, ROHARDT G & KANZOW T. 2021. Observed interannual changes beneath Filchner-Ronne Ice Shelf linked to large-scale atmospheric circulation. *Nat Commun* 12: 1-11.
- HILLEBRAND FL, BREMER UF, FREITAS MW DE, COSTI J, MENDES JÚNIOR CW, ARIGONY-NETO J & SIMÕES JC. 2022. Spectral Linear Mixing Model applied to data from passive microwave radiometers for sea ice mapping in the Antarctic Peninsula. *Geocarto Int* 37: 3141-3166.
- HOLLAND PR, BRUNEAU N, ENRIGHT C, LOSCH M, KURTZ NT & KWOK R. 2014. Modeled trends in Antarctic sea ice thickness. *J Clim* 27: 3784-3801.
- HOLLAND PR. 2014. The seasonality of Antarctic sea ice trends. *Geophys Res Lett* 41: 4230-4237.
- JOHNSON GL, VANNEY JR, ELVERHØI A & LABRECQUE JL. 1981. Morphology of the Weddell sea and southwest Indian Ocean. *Deutsche Hydrografische Zeitschrift* 34: 263-272.
- KERN S & SPREEN G. 2015. Uncertainties in Antarctic sea-ice thickness retrieval from ICESat. *Ann Glaciol* 56: 107-119.
- KERN S, OZSOY-ÇIÇEK B & WORBY AP. 2016. Antarctic Sea-Ice Thickness Retrieval from ICESat: Inter-Comparison of Different Approaches. *Remote Sens* 8: 538.
- KESHAVA N. 2003. A survey of spectral unmixing algorithms. *Lincoln Laboratory Journal*. 14: 55-78.
- KUMAR A, YADAV J & MOHAN R. 2021. Seasonal sea-ice variability and its trend in the Weddell Sea sector of West Antarctica. *Environ Res Lett* 16: 024046.
- KURTZ NT & MARKUS T. 2012. Satellite observations of Antarctic sea ice thickness and volume. *J Geophys Res-Oceans* 117: 1-9.
- KWOK R, ZWALLY HJ & YI D. 2004. ICESat observations of Arctic sea ice: A first look. *Geophys Res Lett* 3: L16401.
- LEE S-K, VOLKOV DL, LOPEZ H, CHEON WG, GORDON AL, LIU Y & WANNINKHOF R. 2017. Wind-driven ocean dynamics impact on the contrasting sea-ice trends around West Antarctica *J Geophys Res* 122: 4413-4430.
- MARTIN S, DRUCKER R, KWOK R & HOLT B. 2004. Estimation of the thin ice thickness and heat fluxes for the Chukchi Sea Alaskan coast polynya from SSM/I data, 1990-2001. *J Geophys Res-Oceans* 109: 1-15.
- MASSOM RA ET AL. 2001. Snow on Antarctic Sea ice. *Rev Geophys* 39: 413-445.
- MASSONNET F, MATHIOT P, FICHEFET T, GOOSSE H, BEATTY CK, VANCOPPENOLLE M & LAVERGNE T. 2013. A model reconstruction of the Antarctic sea ice thickness and volume changes over 1980-2008 using data assimilation. *Ocean Model* 64: 67-75.
- MEIER WN & MARKUS T. 2015. Remote sensing of sea ice. In *Remote Sensing of the Cryosphere*. New York: Wiley Blackwell.
- NAKAYAMA M, CHO K, SHIMODA H, SAKATA T, TANIKAWA T & NISHIO F. 2000. Evaluation of frequency band and polarization of microwave radiometer for observation of first-year ice in the Okhotsk Sea. *JJSSI* 62: 523-535 (in Japanese).
- NAOKI K, UKITA J, NISHIO F, NAKAYAMA M, COMISO JC & GASIEWSKI AJ. 2008. Thin sea ice thickness as inferred from passive microwave and in situ observations. *J Geophys Res-Oceans* 113: 1-11.
- ORSI AH, SMETHIE WM & BULLISTER JL. 2002. On the total input of Antarctic waters to the deep ocean: a preliminary estimate from chlorofluorocarbon measurements *J Geophys Res* 107: 31-1-31-14.
- OZSOY-CICEK B, ACKLEY SF, XIE H, YI D & ZWALLY J. 2013. Sea-ice thickness retrieval algorithms based on in-situ surface elevation and thickness values for application to altimetry. *J Geophys Res-Oceans* 118: 3807-3822.
- PARKINSON CL & CAVALIERI DJ. 2012. Antarctic sea ice variability and trends, 1979-2010. *TC* 6: 871-880.
- PARKINSON CL. 2019. A 40-y record reveals gradual Antarctic sea ice increases followed by decreases at rates far exceeding the rates seen in the Arctic. *PNAS USA*. 116: 14414-14423.
- PAUL S, WILLMES S & HEINEMANN G. 2015. Long-term coastal-polynya dynamics in the southern Weddell Sea from MODIS thermal-infrared imagery. *TC* 9: 2027-2041.
- QUINTANO C, FERNÁNDEZ-MANSO A, SHIMABUKURO YE & PEREIRA G. 2012. Spectral unmixing. *Int J Remote Sens* 33: 5307-5340.
- RENNER AHH & LYTLE V. 2007. Sea-ice thickness in the Weddell Sea, Antarctica: a comparison of model and upward-looking sonar data. *Ann Glaciol*. 46: 419-427.
- SCHOWENGERDT RA. 2006. *Remote sensing: models and methods for image processing*. Burlington: Academic Press.

- SHAPIRO SS & WILK MB. 1965. An Analysis of Variance Test for Normality (Complete Samples). *Biometrika* 52: 591-609.
- SHI Q, YANG Q, MU L, WANG J, MASSONNET F & MAZLOFF MR. 2021. Evaluation of sea-ice thickness from four reanalyses in the Antarctic Weddell Sea. *TC* 15: 31-47.
- SHIMABUKURO YE, DUTRA AC & ARAI E. 2020. Linear Spectral Mixing Model: Theoretical Concepts, Algorithms and Applications of Studies in the Legal Amazon. *RBC* 72: 1170-1199.
- SHIMABUKURO Y & SMITH J. 1991. The least-squares mixing models to generate fraction images derived from remote sensing multispectral data. *IEEE Trans Geosci Remote Sens* 29: 16-20.
- SPREEN G, KALESCHKE L & HEYGSTER G. 2008. Sea ice remote sensing using AMSR-E 89-GHz channels. *J Geophys Res Oceans* 113.
- STRASS VH, ROHARDT G, KANZOW T, HOPPEMA M & BOEBEL O. 2020. Multidecadal warming and density loss in the deep Weddell Sea, Antarctica. *J Clim* 33: 9863-9881.
- SWATHI M, KUMAR A & MOHAN R. 2023. Spatiotemporal evolution of sea ice and its teleconnections with large-scale climate indices over Antarctica. *Mar Pollut Bull* 188: 114634.
- TALLEY LD, PICKARD GL, EMERY WJ & SWIFT JH. 2011. *Descriptive Physical Oceanography: An Introduction*. Amsterdam: Elsevier.
- TATEYAMA K, ENOMOTO H, TOYOTA T & UTO S. 2002. Sea ice thickness estimated from passive microwave radiometers. *Polar Meteorol Glaciol* 16: 15-31.
- TRESHNIKOV AF. 1964. Surface water circulation in the Antarctic Ocean. *Information Bulletin of the Soviet Antarctic Expedition* 5: 81-83.
- TURNER J, BINDSCHADLER R, CONVEY P, DI PRISCO G, FAHRBACH E, GUTT J & SUMMERHAYES C. 2009. *Antarctic Climate Change and the Environment*. Cambridge (UK): Scientific Committee on Antarctic Research.
- TURNER J, MARSHALL GJ, CLEM K, COLWELL S, PHILLIPS T & LU H. 2020. Antarctic temperature variability and change from station data. *Int J Climatol* 40: 2986-3007.
- WENSNAHAN M, MAYKUT GA & GRENFELL TC. 1993. Passive microwave remote sensing of thin sea ice using principal component analysis. *J Geophys Res Oceans* 98: 12453-12468.
- WORBY AP & ALLISON I. 1999. A technique for making ship-based observations of Antarctic sea ice thickness and characteristics: Part I. Observational technique and results. *Antarctic CRC* 14: 1-23.
- WORBY AP, GEIGER CA, PAGET MJ, VAN WOERT ML, ACKLEY SF & DELIBERTY TL. 2008. Thickness distribution of Antarctic sea ice. *J Geophys Res-Oceans* 113: C05S92.
- YI D, ZWALLY HJ & ROBBINS JW. 2011. ICESat observations of seasonal and interannual variations of sea-ice freeboard and estimated thickness in the Weddell Sea, Antarctica (2003-2009). *Ann Glaciol* 52: 43-51.
- YOSHIZAWA E, SHIMADA K & CHO KH. 2018. Algorithm for Flat First-Year Ice Draft Using AMSR2 Data in the Arctic Ocean. *J Atmos Ocean Technol* 35: 2147-2157.
- ZWALLY HJ, COMISO JC, PARKINSON CL, CAVALIERI DJ & GLOERSEN P. 2002a. Variability of Antarctic sea ice 1979-1998. *J Geophys Res-Oceans* 107: 9-1-9-21.
- ZWALLY HJ ET AL. 2002b. ICESat's laser measurements of polar ice, atmosphere, ocean, and land. *J Geodyn* 34: 405-445.
- ZWALLY HJ, YI D, KWOK R & ZHAO Y. 2008. ICESat measurements of sea ice freeboard and estimates of sea-ice thickness in the Weddell Sea. *J Geophys Res-Oceans* 113: 1-17.

How to cite

HILLEBRAND FL, FREITAS MWD, BREMER UF, ABRANTES TC, SIMÕES JC, MENDES JÚNIOR CW, SCHARDONG F & ARIGONY-NETO J. 2023. Concentration and thickness of sea ice in the Weddell Sea from SSM/I passive microwave radiometer data. *An Acad Bras Cienc* 95: e20230342. DOI 10.1590/0001-376520230230342.

*Manuscript received on March 26, 2023;
accepted for publication on August 27, 2023*

FERNANDO LUIS HILLEBRAND^{1,2}

<https://orcid.org/0000-0002-0182-8526>

MARCOS W.D. DE FREITAS^{2,3,4}

<https://orcid.org/0000-0001-9879-2584>

ULISSES F. BREMER^{2,3,4}

<https://orcid.org/0000-0003-0519-5807>

TALES C. ABRANTES³

<https://orcid.org/0000-0003-0773-1458>

JEFFERSON C. SIMÕES^{2,4}

<https://orcid.org/0000-0001-5555-3401>

CLÁUDIO W. MENDES JÚNIOR^{2,3,4}

<https://orcid.org/0000-0003-1745-348X>

FREDERICO SCHARDONG¹

<https://orcid.org/0000-0003-4492-163X>

JORGE ARIGONY-NETO⁵

<https://orcid.org/0000-0003-4848-2064>

¹Instituto Federal de Educação, Ciência e Tecnologia do Rio Grande do Sul/IFRS, Rodovia RS-239, Km 68, 3505, 95700-000 Rolante, RS, Brazil

²Universidade Federal do Rio Grande do Sul/UFRGS, Centro Polar e Climático, Av. Bento Gonçalves, 9500, Prédio 43136, Salas 208 e 210, 91501-970 Porto Alegre, RS, Brazil

³Universidade Federal do Rio Grande do Sul/UFRGS, Programa de Pós-Graduação em Sensoriamento Remoto, Av. Bento Gonçalves, 9500, Prédio 44202, Setor 5, 90501-970 Porto Alegre, RS, Brazil

⁴Universidade Federal do Rio Grande do Sul/UFRGS, Instituto de Geociências, Av. Bento Gonçalves, 9500, 90501-970 Porto Alegre, RS, Brazil

⁵Universidade Federal do Rio Grande/FURG, Instituto de Oceanografia, Av. Itália, s/n, Km 8, 96201-900 Rio Grande, RS, Brazil

Correspondence to: **Fernando Luis Hillebrand**

E-mail: fernando.hillebrand@rolante.ifrs.edu.br

Author contributions

Tales Camargos Abrantes and Frederico Schardong were responsible for organizing and pre-processing the data from the remote sensors. Fernando Luis Hillebrand and Marcos Wellausen Dias de Freitas were responsible for the manuscript's modeling, statistical analysis, and writing. Ulisses Franz Bremer, Jefferson Cardia Simões, Cláudio Wilson Mendes Júnior, and Jorge Arigony-Neto performed the pre-analysis, discussion of the results, and final revision of the manuscript.

